RESEARCH ARTICLE

Solar RRL

www.solar-rrl.com

Epitaxially Grown p-type Silicon Wafers Ready for Cell Efficiencies Exceeding 25%

Clara Rittmann, Florian Schindler, Armin Richter, Tim Niewelt, Hannah Stolzenburg, Bernd Steinhauser, Jonas Dalke, Marion Drießen, Charlotte Weiss, Stefan Janz, and Martin C. Schubert*

Combining the advantages of a high-efficiency solar cell concept and a low carbon footprint base material is a promising approach for highly efficient, sustainable, and cost-effective solar cells. In this work, we investigate the suitability of epitaxially grown p-type silicon wafers for solar cells with tunnel oxide passivating contact rear emitter. As a first proof of principle, an efficiency limiting bulk recombination analysis of epitaxially grown p-type silicon wafers deposited on high quality substrates (EpiRef) unveils promising cell efficiency potentials exceeding 25% for three different base resistivities of 3, 14, and 100 Ω cm. To understand the remaining limitations in detail, concentrations of metastable defects Fe_i, CrB and BO are assessed by lifetime-calibrated photoluminescence imaging and their impact on the overall recombination is evaluated. The EpiRef wafers' efficiency potential is tracked along the solar cell fabrication process to quantify the impact of high temperature treatments on the material quality. We observe large areas with few structural defects on the wafer featuring lifetimes exceeding 10 ms and an efficiency potential of 25.8% even after exposing the wafer to a thermal oxidation at 1050 °C.

1. Introduction

Epitaxial growth in comparison to ingot crystallization has various advantages: more easily and accurately adjustable doping concentration and wafer thickness, as well as absence of oxygen during epitaxial growth. Furthermore, kerfless wafering using epitaxially grown layers 'EpiWafers' on reusable substrates with a stack of porous silicon detachment layers, offers a significant material-, energy- and cost-reduction.[1–3] Until now, solar cells of p-type Si EpiWafers have shown efficiencies up to 19.7% and of n-type Si EpiWafers up to 22.5%.[4–6] In this contribution, we demonstrate the suitability of this low cost and low carbon footprint material for fabrication of solar cells with highest efficiencies exceeding 25%. This is realized by a proof of concept focusing only on the quality of the epitaxial growth itself by epitaxially depositing 'EpiRef' wafers on ideal, chemically–mechanically polished substrates that are removed by grinding. This procedure allows for neglecting quality limitations induced by the porous silicon detachment layer in the first place. The influence of the properties of the porous silicon detachment layer on EpiWafer's quality has been studied by various groups and is still ongoing.[7–9] Again for EpiWafers, the influence of the substrate itself as well as of the reactor for epitaxial growth has been discussed.[10] In this contribution, we demonstrate in turn that EpiRef wafers are well suited for high-efficiency TOPCoRE cells which have just recently shown efficiencies up to 26% for float-zone material.[11]

Based on our earlier observations, we systematically optimize the efficiency potential on state-of-the-art epitaxially grown silicon wafers by e.g., finding the best suited base resistivity and thickness in this contribution.[8] As the base resistivity (i.e., the doping concentration) has a strong influence on the cell performance which in turn depends on the material specific impurity mix, it is of high importance to understand the still limiting mix of bulk defects in epitaxially grown material.[12,13] Despite of some research on epitaxially grown p-type Si in direct comparison to epitaxially grown n-type Si, the impurity mix in p-type epitaxial silicon is neither investigated nor known yet.[14] Therefore, we investigate EpiRef wafers of three different base resistivities: 3, 14, and 100 Ω cm. We specifically focus on stuctural defects as well as the metastable defects interstitial iron Fe_i, chromium-boron CrB, and boron–oxygen BO all of which are present under illumination.

Further, the impact of high temperature treatment on EpiRef wafers is discussed as a first step towards successful cell

C. Rittmann, F. Schindler, A. Richter, T. Niewelt, H. Stolzenburg, B. Steinhauser, J. Dalke, M. Drießen, C. Weiss, S. Janz, M. C. Schubert
Fraunhofer Institute for Solar Energy Systems (ISE)
79110 Freiburg, Germany
E-mail: clara.rittmann@ise.fraunhofer.de

T. Niewelt
Laboratory for Photovoltaic Energy Conversion
Department of Sustainable Systems Engineering (INATECH)
University of Freiburg
79110 Freiburg, Germany

T. Niewelt
School of Engineering
University of Warwick
Coventry CV4 7AL, UK

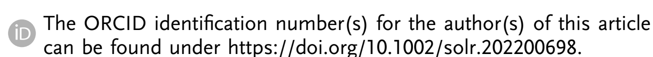
The ORCID identification number(s) for the author(s) of this article can be found under https://doi.org/10.1002/solr.202200698.

© 2022 The Authors. Solar RRL published by Wiley-VCH GmbH. This is an open access article under the terms of the Creative Commons Attribution License, which permits use, distribution and reproduction in any medium, provided the original work is properly cited.

DOI: 10.1002/solr.202200698

2367198x, 0, Downloaded from https://onlinelibrary.wiley.com/doi/10.1002/solr.202200698 by Test, Wiley Online Library on [07/12/2022]. See the Terms and Conditions (https://onlinelibrary.wiley.com/terms-and-conditions) on Wiley Online Library for rules of use; OA articles are governed by the applicable Creative Commons License

fabrication of high-efficiency cells since the state-of-the-art TOPCoRE cell fabrication requires several processing steps at 1050 °C.[11] The high temperature treatment is performed at EpiRef wafers with optimized doping concentration and thickness determined based on the results of the doping variation.

2. Experimental Section

2.1. Epitaxial Growth and Sample Preparation

We grow a variety of EpiRef wafers with a chemical vapour deposition (CVD) batch reactor at atmospheric pressure from LPE (PE 2061S) 'PEpi'. For epitaxial growth of p-type Si, we use trichlorosilane and diborane diluted in hydrogen as precursor gases. Ten substrate wafers per batch are inductively heated to a constant and homogeneously distributed process temperature of 1120 °C for 140 min of epitaxial growth with a growth rate of ≈ 1 μm min^{-1}. The samples are mounted vertically in a custom-built susceptor capable for wafer sizes up to M2 as depicted in **Figure 1**a.

The basic concept of EpiRef wafers as references for the epitaxial growth itself is illustrated in Figure 1b. By investigating EpiRef wafers, we can primarily focus on the quality limitations of the epitaxial growth independent from limitations induced by a porous silicon detachment layer which is necessary for EpiWafer produced by kerfless wafering.[15]

We use round, chemically–mechanically polished, p-type Cz-Si wafers with a resistivity of 2.5 Ω cm and a diameter of 150 mm as substrates. After epitaxial growth, the substrate is removed within a diameter of 100 mm by grinding, namely TAIKO-grinding performed by Disco Hi-Tec Europe GmbH, which leaves a 25 mm broad rim for increased mechanical stability. Then, the samples are etched for 5 min with 30% KOH at 80 °C to remove grinding residuals as well as surface damage sufficiently by taking off about 6 μm material on both sides.[16] To produce cell precursors, the wafers are further chemically cleaned and finally passivated with Al_2O_3 deposited by plasma-assisted atomic layer deposition (ALD) at 180 °C for 78 cycles, resulting in 10 nm thick layers on both sides, in a single wafer reactor (Oxford Instruments, OpAL).[17] A forming gas anneal at 425 °C for 25 min activates the Al_2O_3 surface passivation. The resulting sample set consists of EpiRef wafers with a final thickness of 110 μm and three different base resistivities of 3, 14, and 100 Ω cm. For the defect analysis presented in this contribution, we focus on results of three EpiRef wafers exemplarily: one of each base resistivity. The impact of high temperature treatment on EpiRef wafers is investigated on another 100 Ω cm EpiRef wafer, which is slightly thicker with about 150 μm. The quality of EpiRef wafers can vary slightly in between two runs of epitaxial growth and also within one run depending on the EpiRef wafer's position in the susceptor during epitaxial growth. A systematical analysis of this variance is ongoing. All here discussed findings are in line with lifetime measurements and brightfield imaging after defect selective etching for other experiments on epitaxially grown wafers deposited in our reactor 'PEpi'.

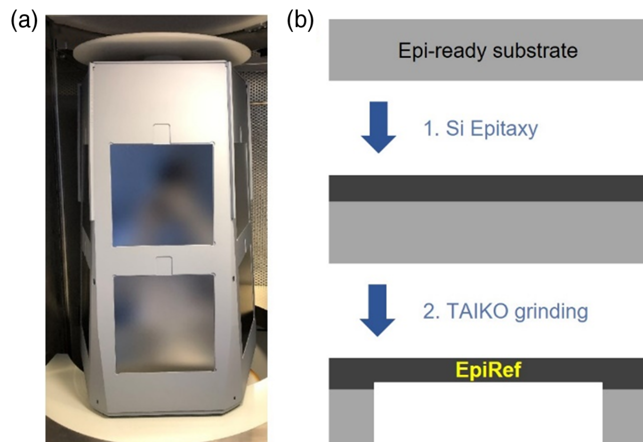

Figure 1. a) Custom-built, M2 size susceptor used in commercial CVD batch-reactor PE2061 from LPE ('PEpi') of microelectronic standard. b) Concept of EpiRef wafer production as a reference for the quality of epitaxial growth.

2.2. Characterization Methods

In this contribution, spatially resolved and injection-dependent minority charge carrier lifetime measurements provide the basis of efficiency analysis and analysis of material quality limitation caused by structural defects and by metastable defects Fe_i, CrB, and BO. For this purpose, lifetimes are measured by photoluminescence imaging (PLI) calibrated with modulated photoluminescence in Fraunhofer ISE's modulum setup at an illumination intensity ranging from 0.001 up to 2.5 sun equivalents.[18,19] The PLI results are further evaluated by using efficiency limiting bulk recombination analysis (ELBA) and a numerical 2D cell simulation with Quokka 3.[20–22] The applied TOPCoRE cell model features a p-type base and an n-type tunnel oxide passivating contact (TOPCon) stack at the rear surface serving as a back junction, as shown in **Figure 2**.[11] The TOPCon stack consists of a SiO_x layer, doped poly-Si, and a full area metal contact. For ELBA, a TOPCoRE cell model with a front finger grid design featuring 1 mm pitches is applied to all EpiRef wafers independent of their resistivity. Further details of the simulation set-up for ELBA are described by Richter et al.[11] Results of ELBA and spatially averaged, injection dependent lifetimes are discussed in areas free of structural defects on EpiRef as well as in large areas with structural defects to quantify the influence of structural defects on lifetime and efficiency.

Defect concentrations of Fe_i, CrB and BO are determined by PLI using the metastable properties of these defects under illumination and heat treatment.[23] For Fe_i-imaging, PLI after

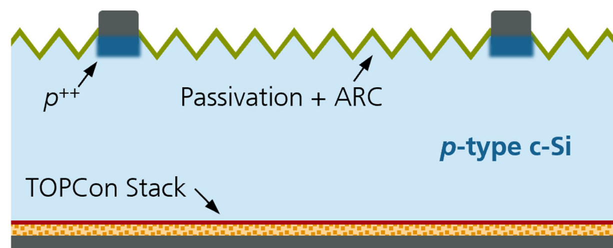

Figure 2. High-efficiency TOPCoRE cell model with p-type base and n-type TOPCon rear junction.

© 2022 The Authors. Solar RRL published by Wiley-VCH GmbH

2367198x, 0, Downloaded from https://onlinelibrary.wiley.com/doi/10.1002/solr.202200698 by Test, Wiley Online Library on [07/12/2022]. See the Terms and Conditions (https://onlinelibrary.wiley.com/terms-and-conditions) on Wiley Online Library for rules of use; OA articles are governed by the applicable Creative Commons License

2367198x, 0, Downloaded from https://onlinelibrary.wiley.com/doi/10.1002/solr.202200698 by Test, Wiley Online Library on [07/12/2022]. See the Terms and Conditions (https://onlinelibrary.wiley.com/terms-and-conditions) on Wiley Online Library for rules of use; OA articles are governed by the applicable Creative Commons License

heat treatment at 80 °C for 10 min (FeB) and after 10 min of illumination at 2.5 sun equivalents (Fe_i) are compared. For CrB-imaging, Cr_i state is generated by heat treatment at 250 °C for 10 min and CrB state is achieved via heat treatment at 100 °C for 60 min. To guarantee well defined states of iron, light induced dissociation of FeB is ensured by 5 min at 2.5 sun equivalents before each measurement. Lastly, for BO-imaging, BO is activated by several days of light soaking and deactivated by heat treatment at 200 °C for 10 min. BO as well as CrB concentrations can only be measured for the 3 Ω cm EpiRef wafers since for lowly doped material the dissociation of Cr_i and activation of BO is insufficient. The detected concentration of CrB is assumed to be the same for all EpiRef wafers' doping concentrations since the chromium content is much smaller than the boron content and hence the doping does not limit the CrB pairing process. In contrast, the BO concentration scales linearly with boron content since the oxygen content is much larger than the boron content.[24,25]

3. Results and Discussion

3.1. Lifetime and Efficiency Potential

Spatially resolved minority carrier lifetime detected at a wide range of illumination gives a first impression on the EpiRef's material quality and allows for efficiency predictions. For EpiRef wafers, PLI exposes areas of spatially homogeneous lifetimes and areas of locally reduced lifetime due to structural defects as consequence of epitaxial growth. In specific, **Figure 3**a–c shows PLI pictures of 3, 14, and 100 Ω cm EpiRef wafers with structural defects visible indicating: 1) vertical slip-lines as accumulations of dislocations caused by thermo-mechanical stresses during epitaxial growth which are visible in the lower parts of the wafers; and 2) stacking faults seen as dots of locally reduced lifetime which are distributed across the whole EpiRef area. The spatial uniformity of the passivation itself is checked by a FZ reference wafer added to each ALD process in the OpAl. Brightfield microscope images after defect selective etching on comparable EpiRef wafers of the same epitaxial growth process confirm that the local lifetime reduction originates from slip-lines and stacking faults.[26] Both defect types are present in the $(6 \times 8)\ \mathrm{cm}^2$ areas marked with blue frames and used for further lifetime evaluation. In contrast, the green frames represent the best 1 cm^2 areas where no slip-lines or stacking faults are present. Here, an additional micro-photoluminescence mapping (μPL) with strongly enhanced resolution (by a factor of ten) confirms that no structural defects below the PLI resolution such as single dislocations are present in these best areas. Thus, they are considered as defect-free in terms of structural artefacts and only limited by fully dissolved impurities. A reduction in measured lifetime within these best areas is still expected due to lateral diffusion of excess charge carriers into the surrounding areas of higher defect concentration and hence higher recombination activity, given the long diffusion lengths exceeding several millimeters. The recombination activity of single structural defects is currently investigated by means of PLI, μPL, as well as brightfield microscopy after defect selective etching and will be presented soon. In this contribution, we only consider the lifetime reducing effect of the combination of all structural defects within the large area.

Injection dependent lifetimes extracted in all areas are in the range of milliseconds at an injection of $\Delta n = 1 \times 10^{15}\ \mathrm{cm}^{-3}$ for all investigated doping concentrations, as shown in **Table 1**. For the 100 Ω cm EpiRef wafer, the measured lifetime is as high as 9 ms in the best area. For all samples the difference in measured lifetime between the best and the large area is (15–30)% attributed solely to structural defects, where the impact of recombination active structural defects is most prominent for the 14 Ω cm EpiRef wafer. Injection dependent measured lifetimes within best areas are plotted in **Figure 4** along with the respective intrinsic limit based on the recently reworked Auger model.[27] The curves exhibit different injection dependencies due to different doping concentration of the EpiRef wafers. Lifetime at low injection was not measurable for the 100 Ω cm EpiRef wafer because of its low doping concentration.

Table 1. Averaged measured lifetimes τ_{eff} evaluated at $\Delta n = 1 \times 10^{15}\ \mathrm{cm}^{-3}$ within large areas as well as best, structural defect-free areas on p-type Si EpiRef wafers indicated in Figure 3. The uncertainty of lifetime measurement is 10%.

Sample	$\tau_{\mathrm{eff,large}}$ [ms]	$\tau_{\mathrm{eff,best}}$ [ms]
3 Ω cm EpiRef	1.2	1.4
14 Ω cm EpiRef	3.2	4.2
100 Ω cm EpiRef	7.5	9.0

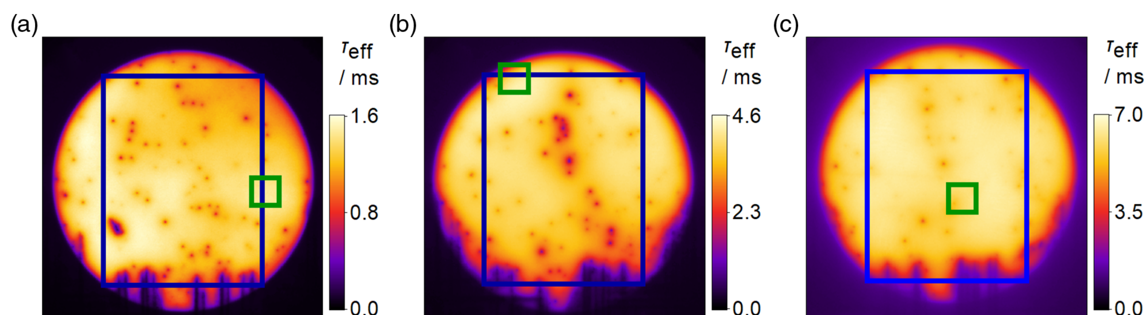

Figure 3. Lifetime calibrated PLI pictures at 0.05 sun equivalents illumination (approx. maximum-power-point) of EpiRef wafer with resistivities of a) 3 Ω cm, b) 14 Ω cm, and c) 100 Ω cm with scales adapted to the lifetime maximum. Blue frames represent defined $(6 \times 8)\ \mathrm{cm}^2$ area including structural defect such as stacking faults and slip-lines. Green frames indicate best, structural defect-free 1 cm^2 areas.

© 2022 The Authors. Solar RRL published by Wiley-VCH GmbH

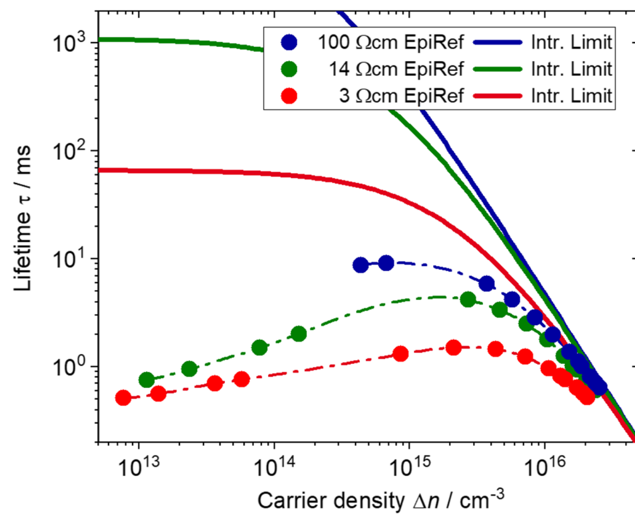

Figure 4. Injection dependent lifetime averaged within the best areas of lifetime calibrated PLI at 0.05 sun equivalents illumination for all investigated boron doped EpiRef wafers (green frames in Figure 3) as well as the corresponding limits of intrinsic bulk recombination. Dashed lines serve as a guide-to-the-eye.

Table 2. Predicted cell efficiencies η evaluated within the large areas and best, structural defect-free areas on p-type Si EpiRef wafers indicated in Figure 3 as well as cell limits η_{limit}.

Sample	η_{large} [%]	η_{best} [%]	η_{limit} [%]
3 Ω cm EpiRef	25.0	25.2	26.5
14 Ω cm EpiRef	25.0	25.4	26.3
100 Ω cm EpiRef	25.4	25.6	26.2

For reliable ELBA results, the injection dependent lifetime close to maximum-power-point (above $\Delta n = 10^{15}\,cm^{-3}$ for all discussed EpiRef wafers) is needed and provided for all EpiRef wafers.

The efficiency potentials calculated by means of ELBA are summarized in **Table 2**, again for best, structural defect-free areas and for the large areas to assess the impact of structural defects quantitatively for the investigated EpiRef wafers. The 100 Ω cm EpiRef wafer features the highest efficiency potential of 25.6% in the best area. As well as for the measured lifetimes, efficiencies within large areas are affected by structural defects. However, within all areas, the determined efficiency potentials are above 25% for all EpiRef wafers. The moderate efficiency potential difference between small areas without structural defects and large areas with structural defects indicates that a certain degree of extrinsic recombination caused by structural defects is tolerable. For EpiRef wafers specifically, we determined densities of structural defects after defect selective etching by software assisted defect counting using the 'analySIS FIVE' image analysis software from Olympus. The results are carefully doublechecked by manually evaluating bright field microscope images. On several EpiRef wafers grown similar to the ones in this study in our reactor 'PEpi', we find that the stacking fault density is less than 1 cm^{-2} and the etch pit density is less than 50 cm^{-2}, independent of the EpiRef wafer's doping concentration. Etch pits indicate dislocations intersecting the sample surface which are accumulated in slip-lines and hence distributed spatially inhomogeneous across EpiRef wafers so that best areas without any dislocations occur. Average expected efficiencies evaluated in these best areas without structural defects show a prominent trend towards higher efficiencies for higher EpiRef wafer's base resistivities. This appears to contradict the reduced theoretical efficiency limit for the TOPCoRE cell concept on higher resistivity material due to increased hole transport losses.[11] Our simulations predict best efficiencies for 100 Ω cm EpiRef wafer being only $-0.6\%_{abs}$ below the cell limit expected for base material solely limited by intrinsic recombination. For the area with structural defects, efficiencies are further reduced, but only by $-0.2\%_{abs}$ enabling still an efficiency potential of 25.4%, which indicates that the influence of recombination at structural crystal defects is low for the high resistivity material.

3.2. Limiting Defects and Material Optimization

To assess why the 100 Ω cm EpiRef is the favorable base material for TOPCoRE cells despite of the cell concept's efficiency optimum at about 3 Ω cm as listed in Table 2, we take a closer look on possibly limiting defects, namely Fe_i, CrB, BO, and structural defects, in terms of their impact on lifetime. Further, surface and intrinsic recombination are considered. All of them contribute to the measured effective lifetime τ_{eff} by $1/\tau_{eff} = 1/\tau_{int} + 1/\tau_{sur} + 1/\tau_{def}$ where the defect lifetime limitation τ_{def} is composed of Fe_i, CrB, BO, structural defects and potentially other unknown contributions: $1/\tau_{def} = 1/\tau_{Fe} + 1/\tau_{CrB} + 1/\tau_{BO} + 1/\tau_{struct} + 1/\tau_{unknown}$. The lifetime limitation due to structural defects is assessed through the difference between the lifetime detected in the large and best, structural defect-free area $1/\tau_{struct} = 1/\tau_{large} – 1/\tau_{best}$ assuming that other defects are distributed homogeneously. Defect lifetime limitations generally depend on the EpiRef wafer's doping concentration and on the defect concentrations: on the 3 Ω cm EpiRef samples, metastable defect imaging results in $[Fe_i]$ of $1 \times 10^9\,cm^{-3}$, [CrB] of $3 \times 10^8\,cm^{-3}$, and $[BO]^*\sigma_{e,BO}$ of $6 \times 10^{-5}\,cm^{-1}$, where no absolute value for the minority carrier capture cross section $\sigma_{e,BO}$ of BO defects is known. Hence, defect concentration [BO] cannot be extracted from lifetime measurements. The defect concentrations of Fe_i and CrB – as long as the boron concentration is orders of magnitudes larger than the Cr_i concentration – should be independent of the doping concentration and can therefore be assumed to be similar for the 14 and 100 Ω cm EpiRef wafer. For BO defects, the concentration is known to scale linearly with doping concentration and quadratically with $[O_i]$.[24,25] To obtain the oxygen concentration, secondary ion mass spectroscopy (SIMS) was performed externally by RTG Mikroanalyse GmbH using the Cameca ims 4f-E6 set-up with a positively charged primary ion beam of cesium Cs^+ (at 14.5 keV) under vacuum condition with (2–5) $\times 10^{-10}$ mbar. For each measurement, a 1 μm deep depth profile of the oxygen concentration was obtained within a sputtering region (90 × 90) μm^2. EpiRef wafers revealed oxygen concentrations of $1 \times 10^{17}\,cm^{-3}$ on the backside, being in contact to

© 2022 The Authors. Solar RRL published by Wiley-VCH GmbH

2367198x, 0, Downloaded from https://onlinelibrary.wiley.com/doi/10.1002/solr.202200698 by Test, Wiley Online Library on [07/12/2022]. See the Terms and Conditions (https://onlinelibrary.wiley.com/terms-and-conditions) on Wiley Online Library for rules of use; OA articles are governed by the applicable Creative Commons License

the substrate during epitaxial growth, and 4×10^{16} cm^{-3} on the frontside. The difference between front- and backside concentration suggests an in-diffusion of oxygen from the Cz-Si substrate wafer into the EpiRef wafer during epitaxial growth. Still, the oxygen content in EpiRef wafers is well below typical concentrations in Cz-Si of (5–10) $\times 10^{17}$ cm^{-3} but above typical concentrations in float-zone Si of (1–5) $\times 10^{16}$ cm^{-3}.[28–30] It is important to point out that the backside of the EpiRef wafer does not represent exactly the substrate-epilayer interface but a position within the epilayers close to the interface due to TAIKO-grinding and etching during sample preparation. The oxygen concentration at the interface is expected to be even higher due to the enhanced oxygen concentration within the Cz-Si substrate. The found oxygen concentrations within EpiRef wafers are well in line with the amount of recombination via BO defects observed by PLI.[31] To determine the influence of the defects on the lifetime, the lifetime limitation curves are calculated using the corresponding models: A surface saturation current J_0 of 2 fA cm^{-2} is assumed based on previous experiments with FZ Si wafers using the same Al_2O_3 deposition process. The intrinsic recombination is calculated based on the reworked Auger-model from Niewelt.[27] Injection dependent lifetimes for these findings and assumptions are presented in **Figure 5** together with measured lifetimes averaged within the large and best area. The difference between the sum of all determined limiting factors (green dashed line) and the measured lifetime within the best area without structural defects (green solid line), highlighted by a green area fill in Figure 5, represents yet unknown limitations.

In turn, the difference between the limitations of the large area and best area, highlighted by a blue area fill, are assigned to structural defects. It is important to note that the measured lifetime within the best area is more strongly affected, hence reduced, by outward diffusion of charge carriers than the large area. Therefore, the lifetime and hence also efficiency limitations caused by structural defects are slightly underestimated at lower Δn, whereas the unknown limitations are potentially even lower than depicted. Defect lifetime limitations τ_{def} of structural defects and of unknown limitations increase with increasing base resistivity (decreasing doping concentration, respectively), as well as the defect lifetime limitations of Fe_i, CrB, and BO. Especially τ_{BO} increases by two orders of magnitude due to the linear scaling with the boron content.

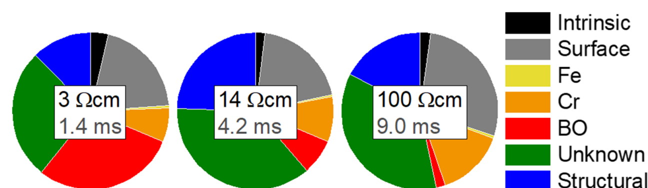

Figure 6. Shares of recombination mechanisms evaluated at $\Delta n = 1 \times 10^{15}$ cm^{-3} in EpiRef wafer depending on the material's resistivity of 3, 14, and100 Ω cm. Measured lifetime at $\Delta n = 1 \times 10^{15}$ cm^{-3} is added in grey.

The relative contributions of the different recombination channels to the total recombination at $\Delta n = 1 \times 10^{15}$ cm^{-3} are visualized in **Figure 6**. We chose a comparison at identical injections Δn to unveil the material's loss mechanisms independent of a certain solar cell design. Please note that for the TOPCoRE cell concept investigated in this work this injection level is close to maximum-power-point (MPP)-conditions for the 3 Ω cm material, whereas with increasing resistivity the MPP shifts towards higher excess charge carrier concentrations. A comparison at injection levels close to the resistivity-specific MPP-conditions is presented later in this chapter. The graphs in Figure 6 depict the relative contributions but not the absolute recombination rate which is largest for the 3 Ω cm showing the lowest lifetime. Again, most prominent is the drop of the influence of BO for EpiRef wafers with increasing base resistivity due to the linear scaling of the BO concentration with the boron content. For the 3 Ω cm sample more than 1/4 of the total recombination can be attributed to BO whereas its influence almost vanishes for the 100 Ω cm EpiRef wafer. The reduction of BO's impact results automatically in larger shares of the other recombination channels such as surface recombination or recombination due to chromium defects. However, this does not mean that their absolute concentration is essentially increased being first of all attributed to the graphical representation of relative recombination mechanism. Further, the impact of structural defects in 14 Ω cm EpiRef wafer is slightly enhanced compared to the other wafers which is attributed to a

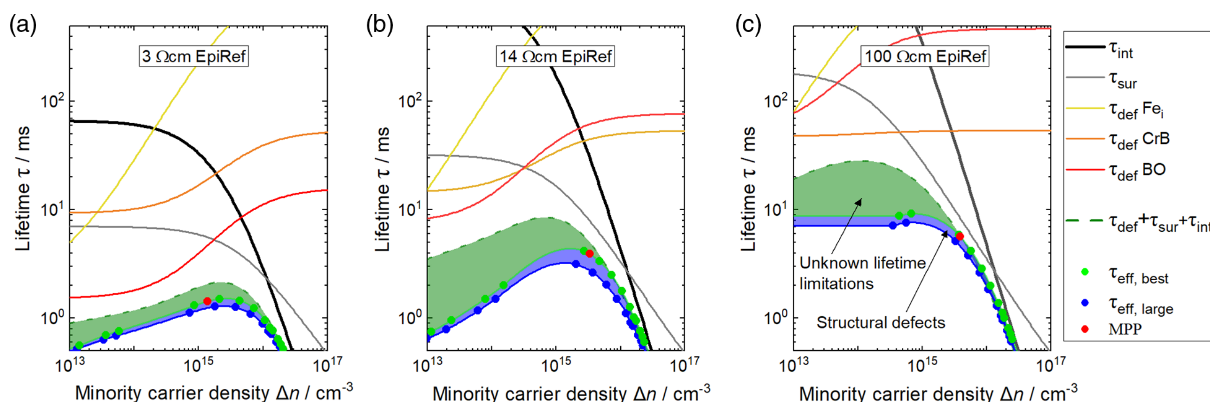

Figure 5. Injection dependent lifetime evaluated in large areas (blue markers) and best areas (green markers) without structural defects as well as lifetimes of the detected lifetime limiting defects for the a) 3 Ω cm, b) 14 Ω cm, and c) 100 Ω cm EpiRef wafer. The blue area indicates recombination at structural defects and the green area yet unknown recombination mechanisms.

© 2022 The Authors. Solar RRL published by Wiley-VCH GmbH

2367198x, 0, Downloaded from https://onlinelibrary.wiley.com/doi/10.1002/solr.202200698 by Test, Wiley Online Library on [07/12/2022]. See the Terms and Conditions (https://onlinelibrary.wiley.com/terms-and-conditions) on Wiley Online Library for rules of use; OA articles are governed by the applicable Creative Commons License

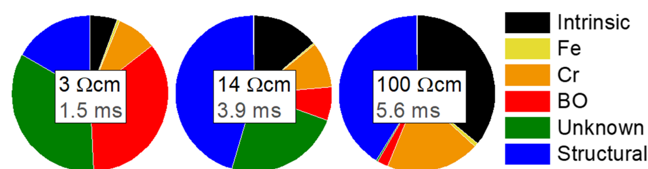

Figure 7. Shares of recombination mechanisms (without surface recombination) evaluated at the estimated MPP condition Δn_{MPP} for the TOPCoRE cell for 3, 14, and 100 Ω cm EpiRef wafer. Measured lifetime at MPP is added in grey.

sample-specific higher density of structural defects within the large area. Apart from BO content and structural defects, the relative material quality limitations are similar between the compared samples independent of the doping concentration.

The recombination shares relevant for a TOPCoRE cell are shown in **Figure 7**. Here, the lifetimes are evaluated at the maximum-power points located at excess charge carrier densities Δn_{MPP} of $1.4 \times 10^{15}\,\text{cm}^{-3}$ for the 3 Ω cm EpiRef wafer, $3.2 \times 10^{15}\,\text{cm}^{-3}$ for the 14 Ω cm EpiRef wafer, and $3.8 \times 10^{15}\,\text{cm}^{-3}$ for the 100 Ω cm EpiRef wafer determined by ELBA and indicated in Figure 5 by red markers. Further, the surface recombination is neglected since the Al_2O_3 passivation of the EpiRef wafer does not represent surface recombination properties in a TOPCoRE cell with a textured front surface and a TOPCon passivated back surface. Again, the impact of BO shrinks with increasing base resistivities. In contrast to the recombination shares evaluated at $\Delta n = 1 \times 10^{15}$, the share of intrinsic recombination increases drastically with increasing base resistivity since the injection level of the MPP is higher for higher base resistivity and intrinsic recombination becomes generally more dominant for higher injections. A larger share of intrinsic recombination goes along with a smaller share of extrinsic recombination such as Fe_i, CrB, and BO. Consequently, Δn_{MPP} is higher, which results in a larger Auger recombination contribution (intrinsic recombination), but also a better cell performance. Especially for the best, structural defect-free areas on the EpiRef wafers, the intrinsic recombination dominates since limitations of structural defects vanish per definition. Consequently, the 100 Ω cm EpiRef material is the most promising candidate for high-efficiency solar cells based on the recombination considerations in this work. Our work suggests that such a material would provide performance close to the cell concept's limit in areas free of structural defects. This finding is supported by the discussed ELBA results considering the influence of bulk-conductivity on the potential solar cell efficiency in addition to recombination effects.

In addition to the optimal resistivity of 100 Ω cm, an optimum for the EpiRef wafer's thickness is determined for all investigated samples, again considering the same TOPCoRE solar cell design. **Figure 8** shows simulated solar cell parameters for a thickness variation from 50 to 250 μm. The solar cell parameters are simulated using Quokka3 based on the injection dependent measured lifetime data presented in Figure 4. In general, the open-circuit voltage V_{oc} drops with increasing thickness as a larger bulk volume inherits more recombination. The 100 Ω cm EpiRef wafers exhibit a higher V_{oc} than the other wafers due to lower recombination in lower injection. In contrary, the short-

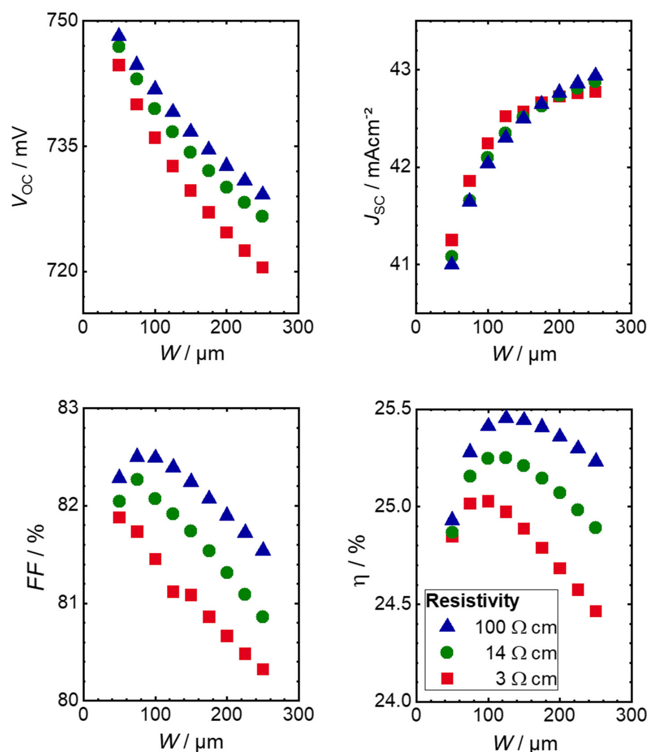

Figure 8. Simulated solar cell parameters V_{oc}, J_{sc}, FF, and η for a wafer thickness W variation based on measured injection dependent lifetime data presented in Figure 4.

circuit current density J_{sc} is almost identical for all investigated wafers and increases with increasing thickness due to improved absorption. The fill factor FF is strongly decreasing with increasing thickness, in particular for thickness $W > 100\,\mu\text{m}$, but is highest for 100 Ω cm material. This is strongly related to the superior injection dependent lifetime around MPP conditions of the 100 Ω cm material. In total, a thickness of 100 μm for 3 Ω cm, of 125 μm for 14 and 100 Ω cm EpiRef wafers is favorable for the specific base resistivity in terms of efficiencies η for the TOPCoRE solar cell design. The 100 Ω cm is predicted to show the best cell performance. In the following, we use EpiRef wafers with 100 Ω cm and 150 μm thickness instead of 125 μm, because of the improved mechanical wafer stability and almost the same predicted cell performance.

3.3. High Temperature Processing of Epitaxial Wafers

To further prove the suitability of epitaxially grown material for TOPCoRE cell fabrication, we study EpiRef wafer's quality before and after high temperature processing. The investigated wafer is a 150 μm thick, 4" wafer cut out of a 100 Ω cm EpiRef wafer with optimized thickness and base resistivity in terms of efficiency. More precisely, we deposited epitaxial layers with a diameter of 150 mm on Cz p-type Si substrates, performed TAIKO-grinding of the substrate within a diameter of 122 mm and subsequently lasered a round 4" diameter sample from the wafer. This sample is etched, cleaned, and passivated in the same way as

© 2022 The Authors. Solar RRL published by Wiley-VCH GmbH

2367198x, 0, Downloaded from https://onlinelibrary.wiley.com/doi/10.1002/solr.202200698 by Test, Wiley Online Library on [07/12/2022]. See the Terms and Conditions (https://onlinelibrary.wiley.com/terms-and-conditions) on Wiley Online Library for rules of use; OA articles are governed by the applicable Creative Commons License

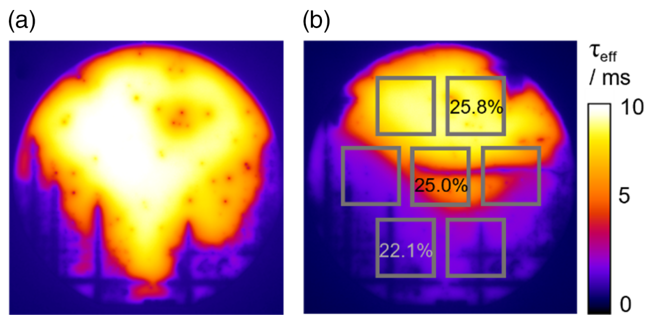

Figure 9. Lifetime calibrated PLI pictures at 0.05 sun equivalents a) before and b) after high temperature processing (oxidation) of 1 h at 1050 °C of epitaxially grown 150 µm thick, 4" EpiRef wafer with a resistivity of 100 Ω cm indicating a quality reduction nearby slip-lines and a subsequent reduction in expected efficiency potential evaluated by ELBA within areas of intended (2 × 2) cm^2 cells. Both images refer to the same minority carrier lifetime scale.

the previously discussed EpiRef wafers. For the fabrication of the TOPCoRE cells high temperature processes are, for instance, required to create the local boron diffusion at the front side metal contacts.[11] To simulate such a high temperature treatment, we exposed the 4" EpiRef wafer to a thermal oxidation at 1050 °C for 1 h in a tube furnace. **Figure 9** displays the impact of the high temperature process on the lifetime of the process reference wafer by PLI at 0.05 sun equivalents illumination, again being close to estimated MPP condition Δn_{MPP}. Before oxidation, spatially resolved PLI at Δn_{MPP} exhibits lifetimes up to 10 ms with areas of locally reduced lifetimes attributed to slip-lines in the lower part of the wafer (see Figure 9a). Injection-dependent lifetime measurements, carried out by quasi-steady-state photoconductance, even reveal large areas with lifetimes above 15 ms at injection levels below $1 \times 10^{15}\,\mathrm{cm}^{-3}$. The measured 150 µm thick, 4" EpiRef wafer exceeds the measured lifetime of the 110 µm thick EpiRef wafer with the same base resistivity used for defect characterization allowing us to assume that the quality of epitaxial growth in the PEpi reactor further increased in the meantime due to process stabilization.

After oxidation, lifetime remains excellent in large areas, but also an area of reduced lifetime evolves around slip-lines in the lower part of the process reference wafer (see Figure 9b). This negative effect on the material quality can either be assigned to impurities dissociating during oxidation that are clustered at the slip-lines or to a multiplication and propagation of dislocations which are clustered within slip-lines.[32] We assume that the area of reduced lifetime after oxidation originates from a propagation of dislocations starting from the slip-lines which will be further investigated by brightfield microscopy after defect selective etching to visualize dislocations. At high temperatures, silicon becomes ductile and internal stress in form of slip-lines propagate under the own weight of the wafer.[33–35] This issue can either be avoided by reducing slip-lines already during epitaxial growth or by reducing thermal stress during high temperature processing by an overall lower temperature budget, slower temperature ramps, or more homogeneous temperature distributions. Epitaxial growth without slip-lines is most likely possible by using a susceptor design of industrial standard with 6"-round pockets instead of the susceptor with M2 quadratic pockets used in this work. Research on high temperature treatment for fabrication of high efficiency solar cells of epitaxially grown Si from our reactor 'PEpi' as well as on the reduction of structural defects within EpiRef wafers is ongoing and a publication considered. However, despite of the quality reduction around the slip-lines, ELBA proves that outstanding efficiencies of 25.8% are still expected for example within the upper right (2 × 2) cm^2 area on the reference wafer.

4. Conclusion

We demonstrate the high quality and purity of epitaxially grown silicon layers from our CVD batch reactor allowing for epitaxial layers suited for fabrication of high-efficiency cells, e.g., based on a TOPCoRE solar cell concept. The investigated EpiRef wafers with base resistivities of 3, 14, and 100 Ω cm feature lifetimes above 1, 4, and 9 ms respectively detected by lifetime calibrated photoluminescence imaging at an injection of $\Delta n = 1 \times 10^{15}\,\mathrm{cm}^{-3}$. We demonstrate an efficiency potential above 25% for all three EpiRef wafers evaluated by efficiency limiting bulk recombination analysis.

We further discuss efficiency losses and lifetime reduction caused by structural defects, and Fe_i–, CrB–, and BO–content in epitaxial layers. Only BO makes up for a significant share of approx. ¼ of total recombination for the 3 Ω cm EpiRef wafer but does not play a major role for recombination in the 14, and 100 Ω cm EpiRef material due to the linear scaling of the BO defect concentration with the boron content. In total, recombination of Fe_i–, CrB–, and BO defects does not affect the efficiency significantly proving the high quality and purity of our epitaxially grown layers.

However, recombination active areas close to structural defects, especially slip-lines, multiply under high temperature treatment and result in local lifetime and efficiency reduction. In our case, these structural defects, originating from epitaxial growth, can be avoided by using another susceptor design. Structural defect-free areas preserve their excellent material quality during high temperature processing. In specific, an EpiRef wafer with 100 Ω cm resistivity and 150 µm thickness used as high temperature process reference exhibits lifetimes close to the intrinsic limit resulting in predicted cell efficiencies of 25.8%, being only 0.5%$_{\mathrm{abs}}$ below the cell limit, within a structural defect-free area after high temperature processing. Therefore, epitaxially grown Si wafers with little structural defects and optimized doping concentration as well as thickness are a very promising candidate for high-efficiency solar cell fabrication with expected efficiencies above 25%.

Acknowledgements

This work was supported by the German Federal Ministry for Economic Affairs and Climate Action (BMWK) and the industry partner within the research cluster PEPSI under contract number 03EE1082C.

Open Access funding enabled and organized by Projekt DEAL.

Conflict of Interest

The authors declare no conflict of interest.

© 2022 The Authors. Solar RRL published by Wiley-VCH GmbH

2367198x, 0, Downloaded from https://onlinelibrary.wiley.com/doi/10.1002/solr.202200698 by Test, Wiley Online Library on [07/12/2022]. See the Terms and Conditions (https://onlinelibrary.wiley.com/terms-and-conditions) on Wiley Online Library for rules of use; OA articles are governed by the applicable Creative Commons License

Data Availability Statement

The data that support the findings of this study are available from the corresponding author upon reasonable request.

Keywords

ELBA, epitaxial silicon, high-efficiency solar cells, material characterization, photovoltaics

Received: July 29, 2022
Revised: September 16, 2022
Published online:

[1] C. Weiss, W. Schreiber, M. Drießen, R. Sorgenfrei, T. Liu, M. Ohnemus, S. Janz, *presented at Proc. 37th European Photovoltaic Solar Energy Conf. and Exhibition*, online, September 2020.
[2] S. Riepe, S. Nold, P. Brailovsky, P. Krenckel, L. Friedrich, S. Janz, R. Preu, *presented at Proc. 37th European Photovoltaic Solar Energy Conf. and Exhibition*, online, September 2020.
[3] ITRPV, International Technology Roadmap for Photovoltaic (ITRPV), https://www.vdma.org/international-technology-roadmap-photovoltaic (accessed: August 2021).
[4] R. Hao, T. S. Ravi, V. Siva, J. Vatus, D. Miller, J. Custodio, K. Moyers, C.-W. Chen, A. Upadhyaya, A. Rohatgi, *presented at Proc. 40th IEEE Photovoltaic Specialist Conf. (PVSC)*, Denver, CO, June 2014.
[5] R. Hao, T. S. Ravi, V. Siva, J. Vatus, I. Kuzma-Filipek, F. Duerinckx, M. Recaman Payo, M. Aleman, E. Cornagliotti, P. Choulat, R. Russell, A. Sharma, L. Tous, A. Uruena, J. Szlufcik, J. Poortmans, *IEEE J. Photovoltaics* **2016**, *6*, 1451.
[6] E. Kobayashi, Y. Watabe, R. Hao, T. S. Ravi, *presented at Proc. 31st European Photovoltaic Solar Energy Conf. and Exhibition*, Hamburg, Germany, September 2015.
[7] M. Karim, R. Martini, H. S. Radhakrishnan, K. van Nieuwenhuysen, V. Depauw, W. Ramadan, I. Gordon, J. Poortmans, *Nanoscale Res. Lett.* **2014**, *9*, 1.
[8] N. Milenkovic, M. Driessen, C. Weiss, S. Janz, *J. Cryst. Growth* **2015**, *432*, 139.
[9] M. K. Sahoo, P. Kale, *Microporous Mesoporous Mater.* **2019**, *289*, 109619.
[10] K. van Nieuwenhuysen, F. Duerinckx, I. Kuzma, D. van Gestel, G. Beaucarne, J. Poortmans, *J. Cryst. Growth* **2006**, *287*, 438.
[11] A. Richter, R. Müller, J. Benick, F. Feldmann, B. Steinhauser, C. Reichel, A. Fell, M. Bivour, M. Hermle, S. W. Glunz, *Nat. Energy* **2021**, *6*, 429.
[12] F. Schindler, B. Michl, P. Krenckel, S. Riepe, J. Benick, R. Müller, A. Richter, S. W. Glunz, M. C. Schubert, *Sol. Energy Mater. Sol. Cells* **2017**, *171*, 180.
[13] A. Richter, J. Benick, F. Feldmann, A. Fell, M. Hermle, S. W. Glunz, *Sol. Energy Mater. Sol. Cells* **2017**, *173*, 96.
[14] C. Gemmel, J. Hensen, S. Kajari-Schröder, R. Brendel, *Energy Procedia* **2016**, *92*, 29.
[15] C. Rittmann, J. Dalke, M. Drießen, C. Weiss, F. Schindler, R. Sorgenfrei, M. C. Schubert, S. Janz, *presented at Proc. 38th European Photovoltaic Solar Energy Conf. and Exhibition*, online, September 2021.
[16] H. Kampwerth, S. Rein, S. W. Glunz, *presented at Proc. 3rd World Conf. on Photovoltaic Energy Conversion (WCPEC)*, Osaka, Japan, May 2003.
[17] A. Richter, J. Benick, M. Hermle, *IEEE J. Photovoltaics* **2013**, *3*, 236.
[18] J. A. Giesecke, M. C. Schubert, B. Michl, F. Schindler, W. Warta, *Sol. Energy Mater. Sol. Cells* **2011**, *95*, 1011.
[19] H. Höffler, F. Schindler, A. Brand, D. Herrmann, R. Eberle, R. Post, A. Kessel, J. Greulich, M. C. Schubert, *presented at Proc. 37th European Photovoltaic Solar Energy Conf. and Exhibition*, online, September 2020.
[20] B. Michl, M. Rüdiger, J. A. Giesecke, M. Hermle, W. Warta, M. C. Schubert, *Sol. Energy Mater. Sol. Cells* **2012**, *98*, 441.
[21] B. Michl, M. Kasemann, W. Warta, M. C. Schubert, *Phys. Status Solidi RRL* **2013**, *7*, 955.
[22] A. Fell, K. C. Fong, K. R. McIntosh, E. Franklin, A. W. Blakers, *IEEE J. Photovoltaics* **2014**, *4*, 1040.
[23] M. C. Schubert, H. Habenicht, W. Warta, *IEEE J. Photovoltaics* **2011**, *1*, 168.
[24] K. Bothe, J. Schmidt, *J. Appl. Phys.* **2006**, *99*, 13701.
[25] S. Y. Lim, F. E. Rougieux, D. Macdonald, *Appl. Phys. Lett.* **2013**, *103*, 92105.
[26] E. S. Supik, Master Thesis, Albert-Ludwigs-Universität Freiburg, **2022**.
[27] T. Niewelt, B. Steinhauser, A. Richter, B. Veith-Wolf, A. Fell, B. Hammann, N. E. Grant, L. Black, J. Tan, A. Youssef, J. D. Murphy, J. Schmidt, M. C. Schubert, S. W. Glunz, *Sol. Energy Mater. Sol. Cells* **2022**, *235*, 111467.
[28] K. G. Barraclough, *J. Cryst. Growth* **1990**, *99*, 654.
[29] R. C. Newman, *J. Phys.: Condens. Matter* **2000**, *12*, R335.
[30] A. Borghesi, B. Pivac, A. Sassella, A. Stella, *J. Appl. Phys.* **1995**, *77*, 4169.
[31] K. Bothe, R. Sinton, J. Schmidt, *Prog. Photovoltaics Res. Appl.* **2005**, *13*, 287.
[32] G. Coletti, P. C. P. Bronsveld, G. Hahn, W. Warta, D. Macdonald, B. Ceccaroli, K. Wambach, N. Le Quang, J. M. Fernandez, *Adv. Funct. Mater.* **2011**, *21*, 879.
[33] A. Danilewsky, J. Wittge, K. Kiefl, D. Allen, P. McNally, J. Garagorri, M. R. Elizalde, T. Baumbach, B. K. Tanner, *J. Appl. Cryst.* **2013**, *46*, 849.
[34] W. S. Yoo, T. Fukada, I. Yokoyama, K. Kang, N. Takahashi, *Jpn. J. Appl. Phys.* **2002**, *41*, 4442.
[35] T. Y. Wang, *J. Cryst. Growth* **2005**, *280*, 16.

© 2022 The Authors. Solar RRL published by Wiley-VCH GmbH

2367198x, 0, Downloaded from https://onlinelibrary.wiley.com/doi/10.1002/solr.202200698 by Test, Wiley Online Library on [07/12/2022]. See the Terms and Conditions (https://onlinelibrary.wiley.com/terms-and-conditions) on Wiley Online Library for rules of use; OA articles are governed by the applicable Creative Commons License